applied sciences

MDPI

Article

Experimental Investigation of Thin-Walled UHPFRCC Modular Barrier for Blast and Ballistic Protection

Michal Mára [1], Candida Talone [1,2], Radoslav Sovják [1,*], Jindřich Fornůsek [1], Jan Zatloukal [1], Přemysl Kheml [1] and Petr Konvalinka [1]

[1] Faculty of Civil Engineering, Czech Technical University in Prague, 166 29 Prague, Czech Republic; michal.mara@fsv.cvut.cz (M.M.); candida.talone@studenti.unich.it (C.T.); jindrich.fornusek@fsv.cvut.cz (J.F.); jan.zatloukal@fsv.cvut.cz (J.Z.); premysl.kheml@fsv.cvut.cz (P.K.); petr.konvalinka@fsv.cvut.cz (P.K.)

[2] Department of Engineering and Geology, University of Chieti-Pescara, 661 00 Pescara, Italy

* Correspondence: sovjak@fsv.cvut.cz

Received: 26 October 2020; Accepted: 4 December 2020; Published: 5 December 2020



Featured Application: The ballistic modular system was developed to serve as a mobile protective barrier against projectile impact and also to mitigate the effect of secondary fragments and explosions. The advantage of the system lies in its very fast assembly at the point of intervention, where no heavy machinery is needed. The whole system can be assembled just by manual manipulation into various shapes. The system is based on reasonable mobility and versatility of the whole solution, which is achieved by combining basic elements according to the needs of the situation.

Abstract: The static response of ballistic panels and also its resistance to blast and ballistic impact is investigated in the framework of this study. By connecting individual ballistic panels together, the protective barrier can be constructed. The protective barrier can be featured as a system with high mobility and versatility that is achieved by linking basic interlocking plate elements together. The resulting protective barrier can be shaped according to many possible scenarios in a wall with various possible opening angles and a small post with the tetragonal base or a larger post with the hexagonal ground plan. The material solution of the protective barrier benefits from the application of ultra-high-performance fibre-reinforced cement-based composites (UHPFRCC), which meets the requirements for enhanced resistance against extreme loads such as blast or impact. Besides, by using UHPFRCC, thin and slender design can be adopted, which is advantageous in many ways. Slender design results in a lower weight, allowing for easy manipulation and replacement. To verify the behavior of the panels, the proposed barrier was subjected to various loadings at different strain rates. The experimental campaign demonstrated that the protective barrier has a reasonable load-bearing capacity and also sufficient resistance against projectile impact and blast effects.

Keywords: protective structure; mobile barrier; cementitious composite; fibres; UHPFRCC; ballistics; blast; experimental testing; quasi-static loading; thin-walled structure

1. Introduction

The proposed protective barrier represents a new protective measure to mitigate the consequences of various extreme load events by providing a lightweight flexible structure that can be built on-site very quickly without the need for heavy machinery. Barriers are based on the utilization of highly resistant and tough ultra-high-performance fibre-reinforced cement-based composite (UHPFRCC), which is well pronounced as a material with increased kinetic energy absorption and dissipation capacity and it is, therefore, well suited as a material for protective structures [1]. Increased energy

absorption and dissipation capacity benefit mainly from the usage of disperse fibre reinforcement. The key phenomenon is that the fibres are being pulled out of the matrix when a fracture occurs, which is much more energy-consuming than pulling out a single rupture of the fibre [2].

The resulting structure was designed as a flexible precast system that is based on high mobility and versatility, which is achieved by interlocking the basic panel elements. The shape of the basic element-protective panel is 1.5 m in length and 0.4 m in width. The panels are 40 mm-thick and the weight of the UHPFRCC panel is less than 55 kg, assuring easy manual operation. There is no rebar reinforcement in the panel and steel fibres are uniformly distributed over the material body. The fibre volume content was set to 1.5%, which was derived from previous studies [3,4] as an optimal trade-off between the price, workability, and resulting performance.

The lightweight and protective mobile barrier benefits mainly from using an ultra-high-performance fibre-reinforced cementitious composite that is well-pronounced for its increased strength, toughness, ductility, and energy absorption and dissipation capacity [5–8]. Besides quasi-static loadings, protective barriers were designed and tested against various extreme load events such as projectile impact and blast. By assembly of individual plates together, several possible structures can be built such as a free-standing wall or closed structure with a tetragonal or hexagonal base. By using locks that are provided at the ends of each plate from both sides, there is no need for any additional fastening material as UHPFRCC plates easily fit together. Moreover, there is no need for a foundation as the system itself is self-bearing. The system of the protective barrier might find its application in the industry in the protection of objects, buildings, and strategic infrastructure; special checkpoints or fortified posts, mobile city barriers, and lightweight barricades for crowd control; protection and support of music and sports events, and safety corridors at shooting ranges and training centres.

A previous study of the ballistic resistance of the UHPFRCC was performed on rectangular slabs with dimensions of 300 × 400 mm and various thicknesses ranging from 40 to 50 mm [4,9–13]. Each impact test was conducted using CZ858 semiautomatic rifle, which is the civilian version of a former Czechoslovak SA-58 military assault rifle [10], and two types of ogive-nosed projectiles were used [11], i.e., a deformable projectile with a full-metal jacket and a soft-lead core (SLC) and a nondeformable projectile with a mild-steel core (MSC) and a smaller lead tip. Both types of projectiles had a mass of 8.04 g with an outer diameter of 7.92 mm, and the inner diameter of the core MSC and SLC was 5.68 mm and 6.32 mm, respectively [9–12]. After the impact, only the core continued penetration [11]. The average muzzle velocity for MSC and SLC was 710 m/s [14]. According to Sovják et al. [9], during the experiment, not all slabs were completely perforated since in some of them the projectile was stuck or the slab was punched but the projectile bounced back. In the cases of MSC projectile impact, an intense shattering and fragmentation occurred; whereas in the SLC projectiles cases, less-intense shattering occurred [11]. The results showed that the implementation of fibers reduced the crater diameter significantly, however, the increase of fibers content beyond 2% has no further effect on crater diameter [9]. Hence, 2% of fibers by volume was found to be optimal.

This research aims to verify the static response of ballistic panels and also its resistance to various man-made threads to which the protective barrier should resist. These are the ballistic impact from a handgun and the blast effect from various charges of TNT at various stand-off distances including contact blast. The static response is described in detail concerning flexure, shear, and punching. The ballistic resistance is addressed in terms of a small firearm showing the effect of an in-service bullet with an impact energy of 450 J. The blast loading is executed both in contact and stand-off modes with various charges ranging from 75 g TNT to 3.6 kg TNT.

2. Materials and Methods

2.1. Ultra-High-Performance Fibre-Reinforced Cementitious Composite

Ultra-high-performance fibre-reinforced cementitious composite (UHPFRCC) presents a highly promising solution for protection against extreme load events such as ballistic and blast. The UHPFRCC

displays enhanced compressive strength and energy absorption and dissipation capacity, which benefits mainly from its super-fine structure by employing disperse fibre reinforcement [15,16]. The dispersed fibres play a crucial role in dissipating the damage from shock loadings [17,18], as the point of impact may occur anywhere within the UHPFRCC body. Due to the uniform distribution of the disperse fibre reinforcement over the material body, the UHPFRCC is well suited for this kind of events. Besides, it has been shown that fibre reinforcement significantly decreases the area and volume of the crater [11,19], thus enhancing its postimpact resistance. UHPFRCC used in the framework of this study was composed of ordinary constituents such as cement, silica fume, silica powder, fine sands, high-range water reducers, water, and fibres (Table 1). The fibres that were used to construct the UHPFRCC were straight and smooth with a length of 14 mm and aspect ratio of 108:1. It has been demonstrated in previous studies that a higher aspect ratio >100:1 results in a significantly higher flexural strength and also in a higher amount of energy dissipated during the fracture [20]. The number of fibres in the material body, which has been set to 1.5% in this study by volume, was derived from a reasonable trade-off between the performance and workability of the fresh mixture. It has been verified that more than 1.5% of fibres by volume turns the workability of the mixture down, which usually results in a decrease in mechanical properties and ballistics performance.

Table 1. Mix design.

Component	Portion
Cement	1
Silica fume	0.1
Silica powder	0.25
Silica sand 0.1–1.2 mm	1.6
High-range water reducers	0.01
Antifoaming agent	0.001

The UHPFRCC base mixture that was used in this study was made using common high-performance concrete constituents and a lower water-to-binder ratio. Table 1 shows the basic components and their relative weight dosages. This type of concrete was used in many previous studies and is described in detail elsewhere [21,22] along with its patent [23].

Compressive strength of the hardened composite was determined on cubes of 100 mm in size by monotonic increments of the load by 0.6 MPa/s. Direct tensile strength was determined by using a dog-bone shaped specimen with a central part 200 mm in length and a reduced cross-section of 50 × 100 mm. The total length of the dog-bone specimen was 750 mm and narrowing of its cross-section was done through a pair of clothoids 100 mm in length and 25 mm in height [12]. The loading was deformation controlled, the loading rate was 0.05 mm/min. The compressive strength and tensile strength were determined to be 149 MPa and 8.3 MPa, respectively.

2.2. Static Response of UHPFRCC Plates Barriers

In the early stage of the research, individual panels were tested as a basic element of the ballistic mobile barrier. The slab is 1.5 m-long and the width of the slab is 0.4 m. The thickness of the slab is 0.04 m, which results in the overall weight of the slab being less than 55 kg. The resulting slabs that were shaped from the UHPFRCC were subjected to several static tests in order to verify their static response to flexure, shear, and punching.

2.2.1. Flexural Strength

Four-point bending configuration was applied for the determination of the flexural strength. The separation of the two points spread the region of bending out from the centre such that a larger portion of the material was tested; moreover, between the two loading points there was a free shear force range with a constant bending moment. Each slab was laid horizontally over two supports,

leaving a free span of 1260 mm. The force was applied by a hydraulic jack to the top of the slab through two separate points of contact placed at a distance of 1/3 of the total free span (Figure 1). Each test was carried by displacement control at a rate of 1 mm/min. Draw-wire displacement sensors were installed in the mid-span on both sides of the specimen (Figure 2) [24]. An average of these measurements was then considered. The load–deflection curve was given in real-time by a data acquisition system capable of digitally recording and storing load and deflection data at a 10 Hz frequency.

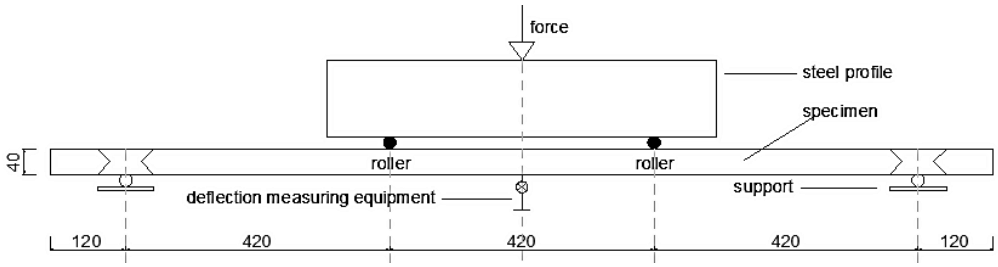


Figure 1. Experimental design (dimensions in mm).



Figure 2. Experimental flexural test campaign.

The tests were performed on specimens after 28 days and 8 specimens were tested to study their bending behavior. The first difference between slabs was regarding their preparation. Some slabs were cast in the laboratory and the others were cast in an industrial unit (Table 2). It is important to underline that the same mix design was used but the drying environment may have differed. The two kinds were easily recognizable thanks to the shape of the corners of the slab, which have been chamfered in the case of panels manufactured in the industrial unit.

Table 2. Specimens characteristics summarization.

Specimen	Status	Casting Place
slab01	undamaged	industrial unit
slab02	undamaged	laboratory
slab03	undamaged	industrial unit
slab04	undamaged	industrial unit
slab05*	*damaged	laboratory
slab06*	*damaged	industrial unit
slab07*	*damaged	industrial unit
slab08	undamaged	industrial unit

The second difference was regarding their damage status: some of the slabs presented damaged conditions post-test due to previous ballistic tests. These slabs had holes and craters of different diameters on the surfaces according to the calibre of firearms used in the previous ballistic tests. For each slab, the holes were concentrated in two different regions that approximately cover 2/3 of

the slab's surface (Figure 3). The calibre was oversized relative to the plate thickness in this case to cause complete perforation and serious damage to the panels on both sides, i.e., both front-side and rear-side craters exist. The craters on the distal face of the panel displayed greater diameter than on the proximal face with shallow cracks. The front-side crater displayed smaller diameter but higher depth due to the compression of the material during the bullets' impact compared to the distal face, where the reflection of the pressure wave occurs.



Figure 3. Predamaged slabs: differences between projectiles' entrance (on the left) and exit (on the right) side.

2.2.2. Shear Strength

The test frame has been designed to impose a pure shear mode on the top of the specimen's surface and to minimize the flexure mode during the opening of the crack. The experimental design was based on indications included in EC2 [25]. Each slab was laid vertically over two supports and fixed by steel supports (Figure 4). The force was applied on a top single point by a hydraulic jack and each test was carried by displacement control at a rate of 1 mm/min. The spherical hinge was placed between the slab and the hydraulic jack to correct eventual geometrical imperfection. Draw-wire displacement sensors were installed on both sides of the specimen and an average of the two measurements was then considered. The load–deflection curve was given in real-time by a data acquisition system capable of digitally recording and storing load and deflection data at a 10 Hz frequency. All the slabs were subjected to a double shear test, one for each side. Steel profiles marked in Figures 4 and 5 were provided to hold the slab at its position.

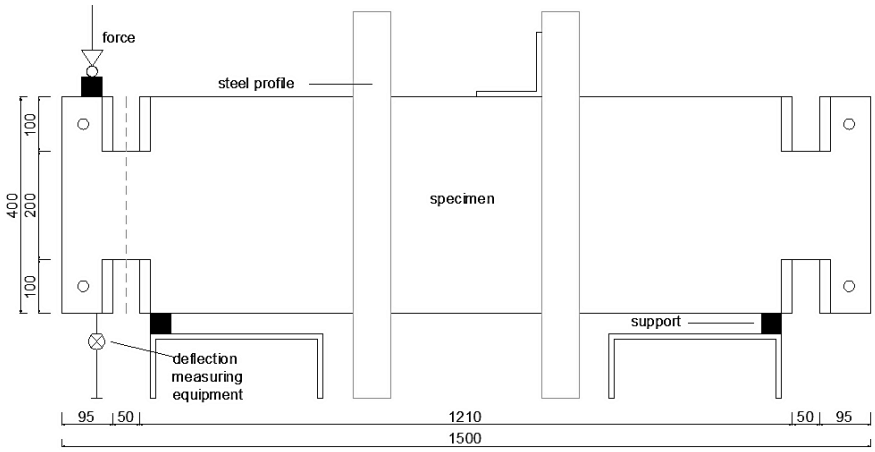


Figure 4. Experimental design (dimensions in mm).



Figure 5. Experimental shear test campaign.

Tests were performed on specimens after 28 days of aging and 3 specimens were tested under shear force (Table 3). The only difference between slabs was about their preparation, as some of them had been cast in the laboratory and the others had been cast in an industrial unit.

Table 3. Specimens' characteristics summarization.

Specimen	Sides	Status	Casting Place
Slab 01	A-B	undamaged	industrial unit
Slab 02	A-B	undamaged	laboratory
Slab 03	A-B	undamaged	laboratory

2.2.3. Punching

For the punching test of UHPFRCC slabs, a special setup was created. The experimental design was based on indications included in EC2 [25]. According to previous studies by Urban et al. [26], Moreillon et al. [27], and Reis et al. [28], a circular pattern is typically chosen, where the slab is supported by eight steel profiles (Figure 6). Each support was braced by four steel struts to avoid inflexion (Figure 7). On the top of each support, a cylinder of 20 mm in diameter was placed so that no punctual cracks could occur in the contact point with the slab and free rotation in the radial direction was allowed (Figure 8).

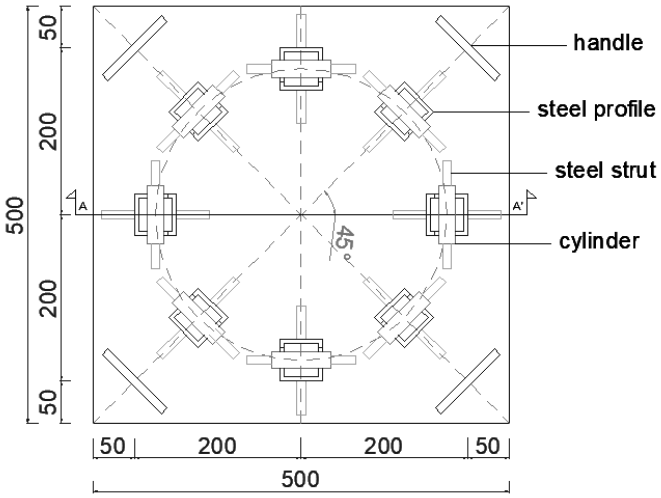


Figure 6. Experimental design of the circular supporting pattern (dimensions in mm).

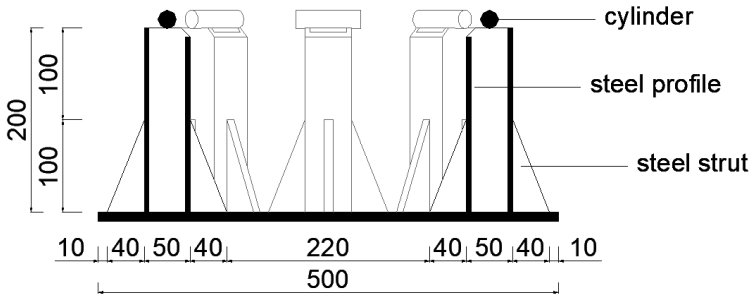


Figure 7. Experimental design of the circular supporting pattern-section AA′ (dimensions in mm).



Figure 8. Circular supporting pattern.

A vertical descending point was applied thanks to a hydraulic jack in correspondence to the centre of the circular pattern. On each slab, two punching tests were performed (Figure 9). The draw-wire displacement sensor was installed under the slab, in the centre of the loaded area.

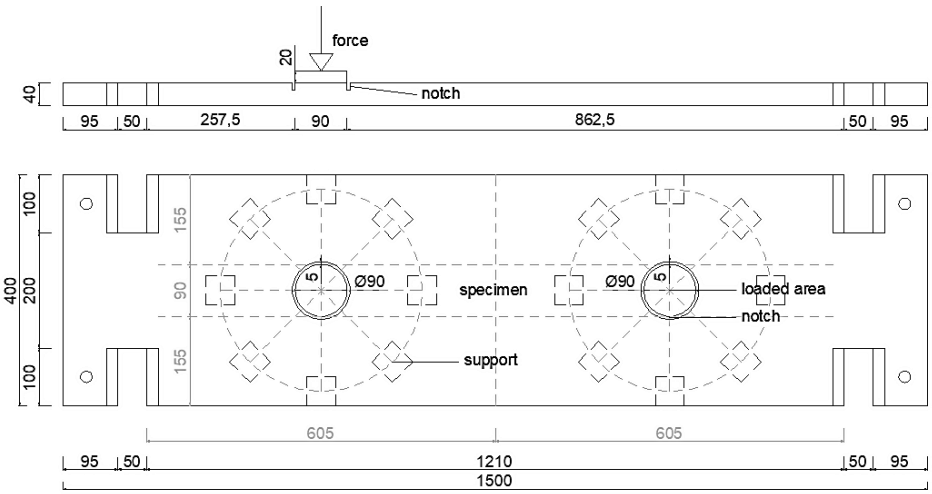


Figure 9. Experimental design (dimensions in mm).

Tests were performed on specimens after 28 days aging (Figure 10) and 3 specimens were subjected to the punching test (Table 4). On each slab, two circular notches had been made some days before the punching test (Figure 11). The notch's depth varied from 11.6 mm to 12.5 mm and it was measured in different points just before the beginning of each test.



Figure 10. Experimental punching test campaign.

Table 4. Specimens characteristics summarization.

Specimen	Status	Casting Place
Slab 01	notched	laboratory
Slab 02	notched	laboratory
Slab 03	notched	laboratory

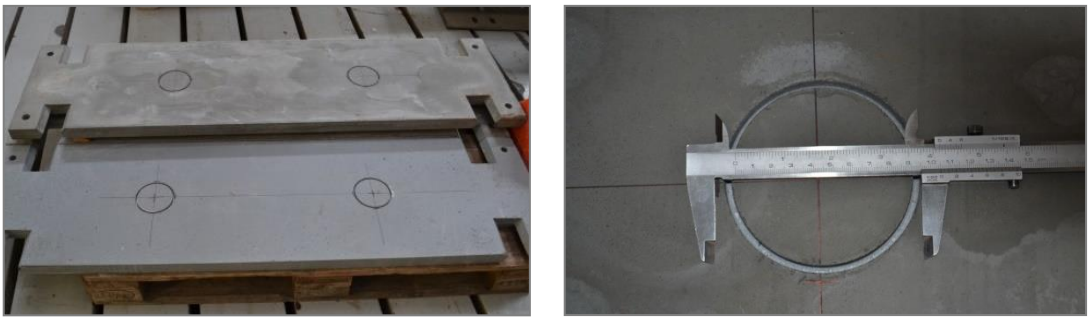


Figure 11. Notched slabs (on the left) and detail of the notch (on the right).

2.3. Blast and Ballistic Loadings

2.3.1. Blast Loading

Explosion tests were performed on individual slabs and also on the entire wall assembly. For individual plates, charges of TNT equivalent were used ranging from 75 g to 2 kg with stand-off distances of up to 1 m. The lowest charge was also used for a contact explosion. The assembly of the wall was 1.8 meters in height, had 4 fields, and the opening angle between the individual fields was 90 degrees. The whole assembly that was built from the UHPFRCC panels was tested against a charge equivalent to 3.6 kg of TNT from a stand-off distance of 3.4 m.

2.3.2. Ballistic Loading

Regarding ballistic tests, a small handgun Luger was used and more than 50 projectiles were fired into one area. The projectile calibre for ballistic tests was a 9 mm, 8 gram, full-metal jacket round-nose bullet. The distance to the slabs was 20 m and the average muzzle velocity for this kind of bullet is 350 m/s. By estimating the velocity loss at 20 m to 17 m/s [29], the impact velocity was about 333 m/s, which determines the impact energy to be around 450 J.

3. Results for Static Loading

3.1. Flexural Test

3.1.1. Peak-Load and Deflection Analysis

The response of undamaged panels consists of three parts, including an elastic branch before the first-peak load, a curved part of strain-hardening from the first-peak load to the peak-load, and a final descending branch of strain-softening (Figure 12).

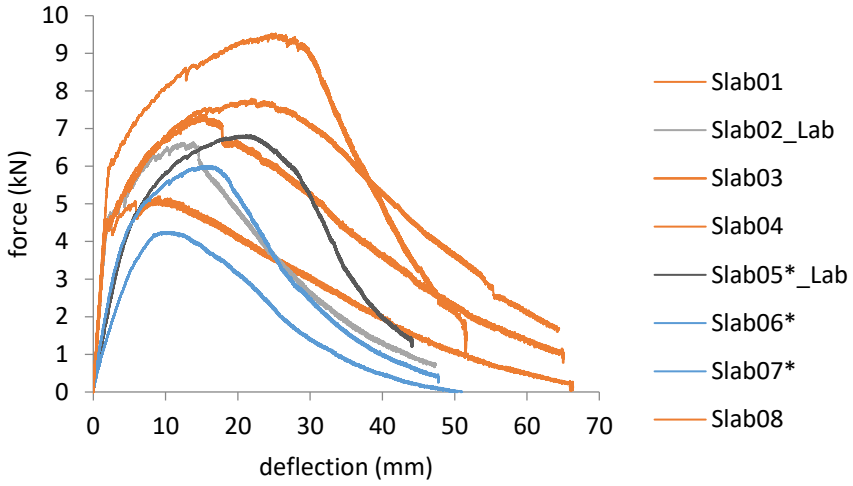


Figure 12. Load–deflection curves (* damaged; _Lab: cast in the laboratory).

The first-peak represents the load corresponding to the first crack, therefore, the specimen no longer has its elastic behavior (Table 5). This value concerns only the undamaged slabs since the damaged ones were already cracked by previous ballistic impact tests.

Table 5. Peak-load average value and standard deviation.

	Undamaged Slabs		**Damaged Slabs**
	1st Peak Load (kN)	**Max Peak Load (kN)**	**Max Peak Load (kN)**
No. of tests	5	5	3
Range	4.7–6.7	5.2–9.5	4.2–6.8
Average	5.1	7.3	5.7
SD	0.9	1.6	1.3

The peak-deflection is the deflection associated with the corresponding peak-load and is an expression of the structural ductility of the element. The ductility is an important quantity for evaluating the flexural performance of concrete since it describes the material's ability to undergo significant plastic deformations before rupture. In this case, the first-peak deflection does not concern the damaged slabs because they are already cracked and do not present a corresponding first-peak load (Table 6).

Table 6. Deflection average value and standard deviation.

	Undamaged Slabs		Damaged Slabs
	1st Peak Defl. (mm)	Max Peak Defl. (mm)	Max Peak Defl. (mm)
No. of tests	5	5	3
Range	2.3–4.0	9–24.7	10.7–21
Average	2.8	16.9	15.8
SD	0.7	6.3	5.2

3.1.2. Fracture Energy

The fracture energy is divided into the energy dissipated during the strain-hardening (G_{fA}) and the energy dissipated during the strain-softening (G_{fB}), calculated as the area under the load–deflection curve. For undamaged slabs, G_{fA} calculation starts from the point of first-peak, where it is assumed that the specimen has lost its elastic behavior under loading and microcracks occur. Instead, for damaged slabs, G_{fA} calculation starts from the beginning of the loading since specimens are already cracked (Table 7).

Table 7. Fracture energy average value and standard deviation.

	Undamaged Slabs			Damaged Slabs		
	G_{fA} (J)	G_{fB} (J)	G_{f_TOT} (J)	G_{fA} (J)	G_{fB} (J)	G_{f_TOT} (J)
No. of tests	5	5	5	3	3	3
Range	32–175	80–164	148–290	31–110	65–75	99–175
Average	97.2	127.9	225.2	70.3	69.5	139.8
SD	56.7	32.5	65.9	39.3	5.3	37.9

3.1.3. Flexural Strength

The engineering stress value experienced just before the failure of the specimen is derived assuming a linear stress distribution (Equation (1)), as indicated in ASTM C 78 (Table 8).

$$\sigma_z^{max} = \frac{M_x}{W} = \frac{M_x}{\frac{b \times h^2}{6}} = \frac{M_x \times 6}{b \times h^2}. \quad (1)$$

Table 8. Flexural strength average value and standard deviation.

	Flexural Strength (MPa)	
	Undamaged Slabs	Damaged Slabs
No. of tests	5	5
Range	10–19	8–13
Average	14.4	11.2
SD	3.1	2.6

3.1.4. Fracture Toughness

According to the ASTM 1018 Standard Test Method [30], fracture toughness is expressed through toughness indexes (Equation (2)) and residual strength factors (Equation (3)).

$$I_N = \frac{Energy\ absorbed\ up\ to\ a\ certain\ multiple\ of\ first\ crack\ deflection}{Energy\ absorbed\ up\ to\ the\ first\ crack}. \quad (2)$$

The subscripts N in these indexes are based on the elastoplastic analogy such that the scheme compares UHPFRCC with a conceptual material behaving in an ideally elastoplastic manner. Additionally, the residual strength factors represent the remaining strength in fibre-reinforced concrete

are derived from the toughness indexes. Residual strength factors state the residual strength factor between indexes I_M and I_N (with $N > M$) in terms of $R_{M,N}$ [31].

$$R_{M,N} = C \times (I_N - I_M), \tag{3}$$

where constant $C = \frac{100}{(N-M)}$ is chosen such that for an ideally elastoplastic material, the residual strength factors assume a value equal to the stress at which the elastic to plastic transition takes place [24].

Given that toughness characterization is based on energy computations, an accurate measurement of deflections is very important, in particular, in the measurement of the first crack. Damaged slabs are not considered because the identification of the first crack is impossible (Tables 9 and 10).

Table 9. Summarization of toughness index data.

	Undamaged Slabs				
	Laboratory	**Ind. Unit**	**Ind. Unit**	**Ind. Unit**	**Ind. Unit**
	slab02	**slab01**	**slab03**	**slab04**	**slab08**
I_5 [-]	4.78	4.21	4.65	4.34	4.63
I_{10} [-]	10.47	8.43	10.05	9.23	10.28
I_{20} [-]	19.70	15.49	19.63	17.36	22.78
I_{30} [-]	24.41	20.31	25.50	-	33.99
I_{40} [-]	-	23.05	28.50	-	41.63
I_{50} [-]	-	24.27	-	-	46.08

Table 10. Summarization of residual strength factors data.

	Undamaged Slabs				
	Laboratory	**Ind. Unit**	**Ind. Unit**	**Ind. Unit**	**Ind. Unit**
	slab02	**slab01**	**slab03**	**slab04**	**slab08**
$R_{5,10}$ [-]	113.88	84.31	108.15	97.77	112.98
$R_{10,20}$ [-]	92.29	70.67	95.75	81.26	125.13
$R_{20,30}$ [-]	47.10	48.19	58.64	-	111.98
$R_{30,40}$ [-]	-	27.36	30.04	-	76.41
$R_{40,50}$ [-]	-	12.23	-	-	44.49

According to the JSCE Standard SF-4 Method [32], the flexural toughness is expressed through flexural toughness factors (Equation (4)), determined from the area below the load–deflection curve (A_{OAFL}) until a deflection of span/150.

$$FT = \frac{A_{OAFL} \times L}{(L/150) \times b \times h^2}. \tag{4}$$

In Equation (4), L is the clear span of the slab, b and h are the width and height of the slab, respectively. Both damaged and undamaged slabs were analyzed for flexural toughness factor (Table 11). However, the flexural toughness factors are specimen geometry-dependent, which makes an exact correlation with the field performance rather difficult [24].

Table 11. Flexural toughness factor average value and standard deviation.

	Flexural Toughness Factor (MPa)	
	Undamaged Slabs	**Damaged Slabs**
No. of tests	5	3
Range	8–12	5–7
Average	9.7	6.3
SD	1.2	1.1

3.2. Shear Test

3.2.1. Peak-Load and Deflection Analysis

Specimens' curves consist of 2 parts, including an elastic branch before the peak-load, and a descending branch until the failure-load (Figure 13). Since that point, a bending behavior occurs and the force decreases linearly.

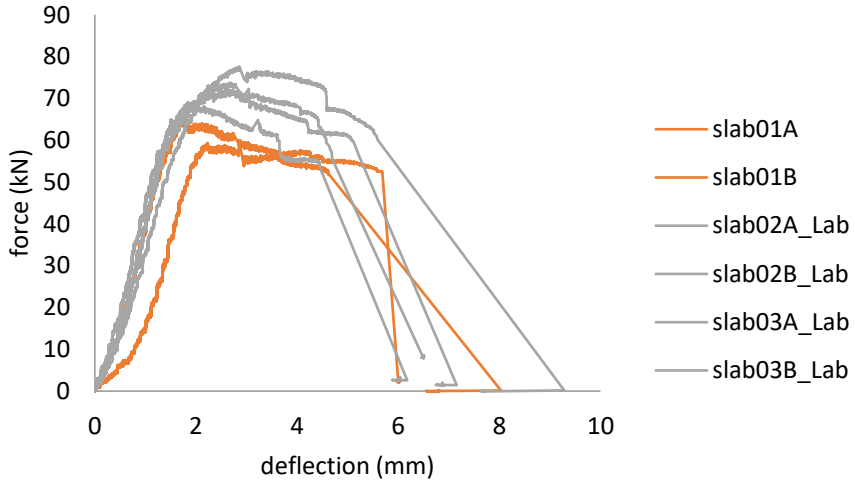


Figure 13. Load-deflection curves (_Lab: cast in the laboratory).

The peak-load represents the load corresponding to the first crack therefore the specimen hasn't its elastic behavior anymore. The failure-load is the point where the rotation of the broken element is starting so it represents the last point for the shear evaluation (Table 12).

Table 12. Peak-load average value and standard deviation.

	Peak Load (kN)	**Failure Load (kN)**
No. of tests	6	6
Range	60–78	52–60
Average	69.6	54.8
SD	6.4	3.0

The peak-deflection is the deflection associated with the corresponding peak-load while the failure-deflection is that associated with the last point of a shear behavior (Table 13).

Table 13. Deflection average value and standard deviation.

	Peak Deflection (mm)	**Failure Deflection (mm)**
No. of tests	6	6
Range	1.4–2.9	4.2–5.3
Average	2.2	4.7
SD	0.6	0.5

3.2.2. Fracture Energy

The fracture energy is calculated as the area under the load–deflection curve from the peak-load to the failure-load, excluding as much as possible, the bending behavior (Table 14).

Table 14. Fracture energy average value and standard deviation.

	Fracture Energy (J)	Fracture Energy (kJ/m^2)
No. of tests	6	6
Range	165–257	16–46
Average	221.5	29.9
SD	51.4	9.8

3.2.3. Shear Strength

The maximum stress (Table 15) that the slab can withstand before failure in a shear mode of loading is calculated according to the Jourawsky formula (Equation (5)).

$$\tau_m(t) = -\frac{T_y \times S^*{}_y(t)}{I_x \times s(t)}. \quad (5)$$

Table 15. Shear strength average value and standard deviation.

	Shear Strength (MPa)
No. of tests	6
Range	11–14.5
Average	13.1
SD	1.2

3.3. Punching Test

3.3.1. Load and Deflection Analysis

The total number of the tested specimens is 3 slabs, each one punched on two loaded-points. The data are available from a total of 6 punching tests. All the slabs were notched and cast in the laboratory (Figure 14).

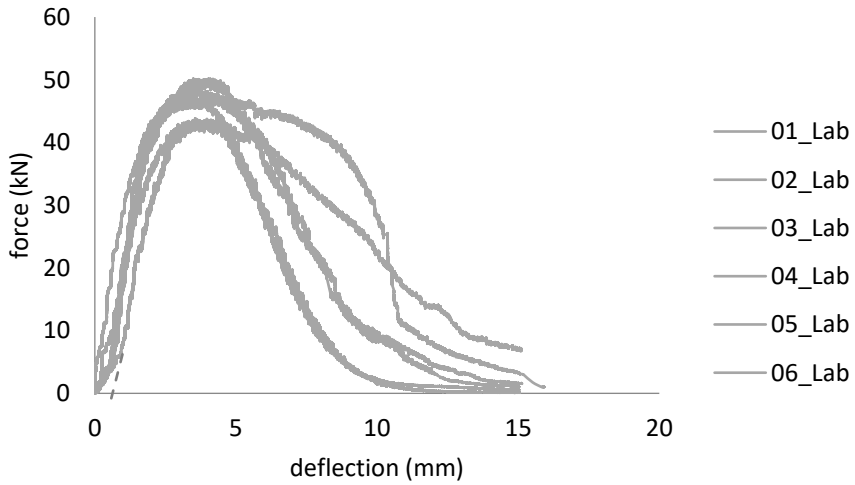


Figure 14. Load–deflection curves (_lab: cast in the laboratory).

All the specimens responded in the same way to the punching test. This is demonstrated by the reasonable standard deviation in the following table (Table 16). The tested slabs fail by punching shear at a force ranging from 44 to 50 kN with a deflection ranging from 3 to 4 mm measured in the center of the truncated cone failure bottom surface. The cracking reaches a distance ranging from 128 to 155 mm from the center of the loaded area with an angle of inclination ranging from 16° to 21°. The cracks' edges are irregular and located two times farther than the theoretical distance 2d.

Table 16. Max-load and corresponding deflection average value and standard deviation.

	Max Load (kN)	Deflection (mm)
No. of tests	6	6
Range	44–50	3–4
Average	46.8	3.4
SD	2.6	0.4

3.3.2. Punching Shear Resistance

The shear resistance of a slab is verified according to EC2 [25] for slabs without shear reinforcement and the influence of a contact surface. The design of punching shear resistance is then given by the following formula (Equation (6)):

$$V_{Rd,c} = C_{Rd,c} \times k \times {f_{ck}}^{\frac{1}{3}} \times \left(\frac{2d}{a}\right) \geq v_{min} \times \left(\frac{2d}{a}\right). \quad (6)$$

- $C_{Rd,c}$ is a constant determined by each country's national annexe but recommended by EC2 [25] as being 0.18;
- $k = 1 + \sqrt{200/d} \leq 2.0$, where d is the depth of the slab in mm;
- f_{ck} is the concrete compressive strength of the slab in MPa;
- a is the distance from the periphery of the loaded area to the control perimeter considered, so in this case, it is equivalent to $2d$;
- $v_{min} = 0.035 \times {k}^{\frac{3}{2}} \times {f_{ck}}^{\frac{1}{2}}$ is the lower limit value of punching shear stress.

Given the slenderness of the tested slabs, the influence of the size parameter k was investigated [33]. Indeed, the theoretical results were obtained considering its limit value $k = 2$ and the actual value for the present case $k = 3.58$.

The experimental shear force that caused punching shear failure can be estimated thanks to the formula below (Equation (7)):

$$v_{Ed,i} = \frac{F_i}{u_i \times d}. \quad (7)$$

- F_i is the shear force applied at the specimen;
- u_i is the perimeter as $2\pi r_i$;
- d is the depth of the specimen.

In this study, the shear stress (Figure 15) is calculated (Table 17) according to the loaded area's perimeter (r = 45 mm) and the control perimeter $2d$ (r = 105 mm).

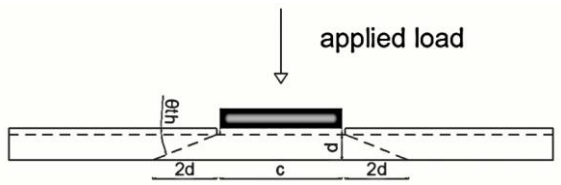


Figure 15. Cracking mode section.

Table 17. Punching shear average value and standard deviation.

	Punching Shear (MPa)	
	r = 45 mm	**r = 105 mm**
No. of tests	6	6
Range	5–6	2–3
Average	5.5	2.4
SD	0.3	0.1

4. Results for Blast and Ballistics

4.1. Results for Blast

The explosive was hung on a special wooden tripod to precisely secure the stand-off distance (SOD) from the tested panels (Figure 16). The explosive was hung with a string to the top of the tripod and the length of the string was set for the exact distance between the explosive and the panel, i.e., SOD. The UHPFRCC panels were similarly supported on two wooden prisms as in the quasi-static flexural test, the clear span was around 1260 mm. Several tripods were constructed to perform all explosion tests at one moment. Configuration of the blast experiment with a specific stand-off distance from the UHPFRCC slab is shown in Figure 16 on the left, and the cumulative explosion over individual plates is shown in Figure 16 on the right. Besides, the wall configuration was tested against 3.6 kg of TNT. The response of the slabs to the blast loading from 75 g of TNT is shown in Table 18 and response to the various charges from a stand-off distance of 1000 mm is shown in Table 19.



Figure 16. Tripod holding a charge (on the left) and simultaneous explosion over individual plates (on the right).

Table 18. Response of ultra-high-performance fibre-reinforced cement-based composites (UHPFRCC) plates to blast loads of 75 g of TNT.

Charge (*g* TNT)	**Contact**	**Stand-off Distance (mm)**				
		250	375	500	750	1000
75	LD	FE	FE	FE	NO	NO

Table 19. Response of UHPFRCC plates to blast loads at 1000 mm stand-off distance (SOD).

SOD (mm)	**Charge (g TNT)**									
	75	150	225	300	400	600	800	1200	1600	2000
1000	NO	NO	NO	NO	FE	FE	FE	GF	GF	GF

That damage that was induced to the slab was classified according to several possible scenarios as local damage (LD), global failure (GF), frontal erosion (FE), and no visible damage (NO).

Local damage (LD) can be characterized by a single crater with complete perforation of the slab (Figure 17 left), showing crater on both sides of the panel. Frontal erosion (FE) might be characterized by a map of smaller craters that are spread across the proximal face of the target where no perforation occurs with no scabbing from the distal face of the panel (Figure 17 right). These craters are usually 1–2 cm in diameter and no more than 5 mm in depth. Global failure (GF) is characterized by the fracture across the entire width of the panel with no residual capacity of the UHPFRCC panel (Figure 18). When no macroscopic damage with no cracks or any erosion is observed on both sides of the panel, the specimen is classified as no visible damage (NO).



Figure 17. Local damage (LD) of the UHPFRCC slab due to the contact explosion from 75 g of TNT (on the left) and frontal erosion (FE) of the UHPFRCC slab from the blast experiment of 400 g of TNT from 1 m (on the right).



Figure 18. Global failure (GF) of the UHPFRCC slab due to the explosion of 1.2 kg of TNT from a stand-off distance of 1 m (on the left) and global failure (GF) of the UHPFRCC slab from the blast experiment of 2 kg of TNT from 1 m (on the right).

The wall that was assembled to be 1.8 m tall was subjected to an explosive charge equivalent to 3.6 kg of TNT from a stand-off distance of 3.4 m. Adjacent panels were tied together with a U-shaped threaded rod to ensure integrity during the blast pressure wave load. The wall withstood the pressure from the blast wave with cracks that developed on the distal face of the UHPFRCC structure (Figure 19). The crack is visible on the middle plates approximately in the middle of its spans. However, the wall remained standing with no secondary fragments that could endanger the surroundings.



Figure 19. Post-test picture showing crack propagation on the distal face of the UHPFRCC wall.

4.2. Results for Ballistics

More than 50 hits from 9 mm Luger projectiles with an impact energy of approximately 450 J were stopped by a single wall of tetragon, i.e., a square post 2 m-tall structure made from UHPFRCC panels. There was no perforation to the distal face of the slabs. Only small craters that were less than 5 mm in depth were observed on the proximal face of the tetragon (Figure 20). It is also important to mention that no scabbing was observed on the distal face of the UHPFRCC panels.



Figure 20. Ballistics loading of the tetragon house (on the left) and the post-test picture showing surface erosion from individual hits on the proximal face of the UHPFRCC plates (on the right).

5. Discussion of Results

Regarding the flexural test, a total of eight panels were tested, some of them were damaged by previous ballistic tests and cast both in the laboratory and in an industrial unit. The behavior of the slabs under flexural loading showed a reasonable ductility of the material. Undamaged slabs reach a first peak-load in the range of 4.7 kN to 6.7 kN with a corresponding deflection ranging from 2.3 mm to 4 mm; while the maximum peak-load lies between 5.2 kN and 9.5 kN with a deflection ranging from 9 mm to 24.7 mm. Damaged panels do not present a first-peak during the application of the force and the curve trend is different from the undamaged panels, so it is only possible to evaluate the maximum force that ranges from 4.2 kN to 6.8 kN with a deflection ranging from 10.7 mm to 21 mm. The casting environment does not have any significant effect on the load resistance.

The investigation of the fracture energy is differentiated between undamaged and damaged slabs. In the undamaged specimens, the fracture energy concerns the dissipation in both a strain-hardening region just before the peak-load and a strain-softening region. The specimens show the fracture energy values ranging from 32 J to 175 J in the strain-hardening region, while in the strain-softening region, the value is much bigger and lies between 80 J and 164 J. The total energy dissipated by the flexural fracture is in the range of 148 J to 290 J or from 9 kJ/m^2 to 17 kJ/m^2 if the cracking area is considered. In the damaged specimens, the fracture energy also concerns dissipation in both regions but there is no recognizable peak-load in the curve, i.e., the differentiation between the two regions is given by the max-load reached by the specimen. The slabs show the fracture energy ranging from 31 J to 110 J in the strain-hardening region, while in the strain-softening region, the fracture energy ranges from 65 J to 75 J. The total energy dissipated by the flexural fracture ranges from 99 J to 175 J or from 8 kJ/m^2 to 22 kJ/m^2 if the cracking area is considered. The smallest value belongs to a single slab cast in the industrial unit, but the number of the specimens considered is not so significant as to allow a correct evaluation of the difference of behavior according to the different casting environment.

The flexural strength is studied as the stress experienced within the material just before the failure and it is derived assuming a linear stress distribution. Its value lies between 10 MPa and 19 MPa for undamaged slabs, and between 8 MPa and 13 MPa for damaged ones.

Lastly, the fracture toughness is analyzed using two different methodologies, i.e., the ASTM 1018 Standard Test Method [30] and the JSCE Standard SF-4 Method [32]. According to the first, toughness characterization is considered only for the undamaged slabs since it is based on the measurement of the first crack. Instead, by the second, it is possible to evaluate the flexural toughness for damaged specimens too. Toughness indexes for each slab, in the beginning, are pretty similar for all the slabs tested; then, as expected, the scatter gets bigger. Residual strength in the material is rationally decreasing. The casting environment does not seem to have significant effects on the toughness characterization.

Regarding the shear test, a total of three slabs were tested on the left and right side, so six shear tests were performed. All the specimens were undamaged and cast both in the laboratory and in an industrial unit. A difference of behavior between the left and the right side of the same slab can be noted and is probably due to a different distribution of the fibres inside the specimen body. The investigation of the fracture energy concerns the dissipation in the postpeak region, after the load-peak but just before the fail-load, when a flexural failure is starting and it is no longer possible to differentiate the shear mechanism. Additionally, in this case, a consideration of the different casting places is not possible because the number of specimens considered is not so significant. The shear strength is studied as the maximum stress that a material can withstand before failure and the shear strength ranges from 11 MPa to 14.5 MPa.

Regarding the punching test, a total of 3 slabs were tested; all the specimens were cast in the laboratory and two notches on their surface were made so as to make two punching tests possible for each slab, so 6 punching tests were realized. The punching shear resistance was investigated according to the influence of the size parameter k, which can be affected because of the slenderness of the specimens. Indeed, the theoretical results were obtained considering its limit value $k = 2$ and the actual value $k = 3{,}58$. The experimental values of the shear resistance have been calculated according to the loaded area's perimeter located at $r = 45$ mm and the control perimeter $2d$ located at $r = 105$ mm from the centre of the loaded area. Comparing the experimental values obtained according to the control perimeter $2d$ with the theoretical ones, they are closer to the value given by the size parameter $k = 3.58$ but values are still far. This means that $k = 2$ yields conservative theoretical values, whereas $k = 3.58$ produces an overestimation of the punching shear strength of the slabs. The average difference between the theoretical and the experimental values is approximately 14%.

During the response of the slabs to the extreme load events, it was experimentally verified that the UHPFRCC panels can withstand a pressure wave from a stand-off distance of 1 meter up to 300 g of TNT with no visible damage and up to 800 g of TNT with visible frontal erosion but no scabbing from the distal face of the panel. Further, it was demonstrated that the ballistic system in terms of a wall 1.8 m in height can withstand a pressure wave from a stand-off distance of 3.4 m delivered by 3.6 kg of TNT. The resulting damage was visible on the distal face of the wall where the crack propagated approximately in the mid-span of the panels in the middle of the height of the wall. However, the wall remains compact and no scabbing occurred on the distal face of the wall, which is very important for personnel operating behind it.

It was further verified that the wall withstood approximately 50 hits from a projectile fired from a short handgun and did not cause any damage to the back of the structure. Only small craters were visible on the front of the wall from the compression of the material upon the impact of the projectile. No material was released from the rear side of the assembly, which is the primary requirement for the safety of intervening units during emergencies.

6. Conclusions and Further Research

This study presented the lightweight protective barrier that may serve primarily for the protection of objects, buildings, and strategic infrastructure; special checkpoints or fortified posts, mobile city barriers, and lightweight barricades for crowd control; protection and support of music and sports events and safety corridors at shooting ranges and training centres. The advantages of the lightweight protective barrier are significantly lower costs compared to equally performing materials and very quick assembly on-site without the need for heavy machinery.

The research presented herein shows favorable material behavior with high mechanical properties and enhanced ballistic resistance. The panel´s resistance to flexure was about 7 kN, where the resistance of the panel that is significantly damaged by previous ballistics is still more than 5 kN. The favorable behavior is mainly achieved by dispersing fibre reinforcement that works extremely well against extreme load events. It was also verified that the UHPFRCC panels display reasonable ballistic response and favorable resistance to the explosion.

Further research will be carried out towards enhancement of the resistance of the UHPFRCC panel by providing additional nonmetallic internal reinforcement and also possibly by providing an additional layer to absolutely suppress both scabbing and spalling from the distal and proximal face of the composite panel, respectively.

Due to the uniform distribution of fibers with a random orientation, its placement may not always be optimal against the applied load, therefore, the next part of the research will also be devoted to the targeted alignment of the fibrous reinforcement. This is possible by the application of magnets that show promising results and may possibly be applied to bigger UHPFRCC elements in the future.

Author Contributions: Conceptualization, C.T. and R.S.; methodology, R.S.; validation, J.F., J.Z., P.K. (Přemysl Kheml), and M.M.; formal analysis, M.M.; investigation, C.T. and P.K. (Přemysl Kheml); resources, J.F.; data curation, M.M.; writing—original draft preparation, C.T.; writing—review and editing, M.M., R.S., and J.Z.; visualization, M.M.; supervision, P.K. (Petr Konvalinka); project administration, J.F.; funding acquisition, P.K. (Petr Konvalinka) and J.F. All authors have read and agreed to the published version of the manuscript.

Funding: The authors gratefully acknowledge the funding by the Ministry of Industry and Trade of the Czech Republic (project number FV10547) and also the funding by the Czech Science Foundation of the Czech Republic (project number 20-00624S).

Acknowledgments: The authors gratefully acknowledge assistance from the technical staff and students at the Experimental Centre from the CTU in Prague who assisted with the tests and participated in the project (project number SGS20/054/OHK1/1T/11).

Conflicts of Interest: The authors declare no conflict of interest.

References

1. Nicolaides, D.; Kanellopoulos, A.; Savva, P.; Petrou, M. Experimental field investigation of impact and blast load resistance of ultra high performance fibre reinforced cementitious composites (UHPFRCCs). *Constr. Build. Mater.* **2015**, *95*, 566–574. [CrossRef]
2. Sovják, R.; Rašínová, J.; Máca, P. Effective fracture energy of ultra-high-performance fibre-reinforced concrete under increased strain rates. *Acta Polytech.* **2014**, *54*, 358–362. [CrossRef]
3. Fornůsek, J.; Mára, M.; Sovják, R.; Zatloukal, J. UHPFRC resistance to projectile impact in dependence on fibre content. In *Materials for Defense—Development, Analysis and Applications*; Fangueiro, R., Sohel, R., Eds.; Springer: Berlin/Heidelberg, Germany, 2020; pp. 63–70.
4. Sovják, R.; Shanbhag, D.; Konrád, P.; Zatloukal, J. Response of thin UHPFRC targets with various fibre volume fractions to deformable projectile impact. *Procedia Eng.* **2017**, *193*, 3–10. [CrossRef]
5. Pyo, S.; Wille, K.; El-Tawil, S.; Naaman, A.E. Strain rate dependent properties of ultra high performance fiber reinforced concrete (UHP-FRC) under tension. *Cem. Concr. Compos.* **2015**, *56*, 15–24. [CrossRef]
6. Wille, K.; El-Tawil, S.; Naaman, A.E. Properties of strain hardening ultra high performance fiber reinforced concrete (UHP-FRC) under direct tensile loading. *Cem. Concr. Compos.* **2014**, *48*, 53–66. [CrossRef]
7. Yoo, D.Y.; Banthia, N. Mechanical properties of ultra-high-performance fiber-reinforced concrete: A review. *Cem. Concr. Compos.* **2016**, *73*, 267–280. [CrossRef]

8. Yoo, D.Y.; Yoon, Y.S.; Banthia, N. Flexural response of steel-fiber-reinforced concrete beams: Effects of strength, fiber content, and strain-rate. *Cem. Concr. Compos.* **2015**, *64*, 84–92. [CrossRef]
9. Máca, P.; Sovják, R.; Konvalinka, P. Mix design of UHPFRC and its response to projectile impact. *Int. J. Impact Eng.* **2014**, *63*, 158–163. [CrossRef]
10. Sovják, R.; Vavřiník, T.; Zatloukal, J.; Máca, P.; Mičunek, T.; Frydrýn, M. Resistance of slim UHPFRC targets to projectile impact using in-service bullets. *Int. J. Impact Eng.* **2015**, *76*, 166–177. [CrossRef]
11. Kravanja, S.; Sovják, R.; Konrád, P.; Zatloukal, J. Penetration resistance of semi-infinite UHPFRC targets with various fiber volume fractions against projectile impact. *Procedia Eng.* **2017**, *193*, 112–119. [CrossRef]
12. Kravanja, S.; Sovják, R. Ultra-high-performance fibre-reinforced concrete under high-velocity projectile impact. Part II. Applicability of prediction models. *Acta Polytech.* **2018**, *58*, 355–364. [CrossRef]
13. Máca, P.; Sovják, R. Resistance of ultra high performance fibre reinforced concrete to projectile impact. In *Structures Under Shock and Impact, Wit Pr/Computational Mechanics*; WIT Press: Southampton, UK, 2012; pp. 261–272. [CrossRef]
14. Sovják, R.; Vavřiník, T.; Máca, P.; Zatloukal, J.; Konvalinka, P.; Song, Y. Experimental investigation of ultra-high performance fiber reinforced concrete slabs subjected to deformable projectile impact. In *Procedia Engineering*; Elseviar: Amsterdam, The Netherlands, 2013; pp. 120–125. [CrossRef]
15. Li, X.; Wang, J.; Bao, Y.; Chen, G. Cyclic behavior of damaged reinforced concrete columns repaired with high-performance fiber-reinforced cementitious composite. *Eng. Struct.* **2017**, *136*, 26–35. [CrossRef]
16. Meng, W.; Khayat, K.H. Improving flexural performance of ultra-high-performance concrete by rheology control of suspending mortar. *Compos. Part B Eng.* **2017**, *117*, 26–34. [CrossRef]
17. Meng, W.; Khayat, K.H. Mechanical properties of ultra-high-performance concrete enhanced with graphite nanoplatelets and carbon nanofibers. *Compos. Part B Eng.* **2016**, *107*, 113–122. [CrossRef]
18. Meng, W.; Khayat, K.H. Effect of graphite nanoplatelets and carbon nanofibers on rheology, hydration, shrinkage, mechanical properties, and microstructure of UHPC. *Cem. Concr. Res.* **2018**, *105*, 64–71. [CrossRef]
19. Kravanja, S.; Sovják, R. Ultra-high-performance fibre-reinforced concrete under high-velocity projectile impact. Part I. Experiments. *Acta Polytech.* **2018**, *58*, 232. [CrossRef]
20. Sovják, R.; Máca, P.; Imlauf, T. Effect of fibre aspect ratio and fibre volume fraction on the effective fracture energy of ultra-high-performance fibre-reinforced concrete. *Acta Polytech.* **2016**, *56*, 319–327. [CrossRef]
21. Bažantová, Z.; Kolář, K.; Konvalinka, P.; Litoš, J.; Petrtýl, M. Controlled hardening of silicate binders for the optimization of high performance composites. In *Key Engineering Materials*; Trans Tech Publications Ltd: Zurich, Switzerland, 2016; pp. 281–285. [CrossRef]
22. Bažantová, Z.; Kolář, K.; Konvalinka, P.; Litoš, J. Multi-functional high-performance cement based composite. *Key Eng. Mater.* **2016**, *677*, 53–56. [CrossRef]
23. Kolář, K.; Bažantová, Z.; Konvalinka, P. *Suchá Prefabrikovaná Směs Multifunkčního Silikátového Kompozitu*; CZ 306663 B3; Industrial Property Office: Prague, Czech Republic, 2015.
24. Banthia, N.; Trottier, J.F. Test methods for flexural toughness characterization of fiber reinforced concrete: Some concerns and a proposition. *ACI Mater. J.* **1995**, *92*, 48–57. [CrossRef]
25. European Committee for Standardization. *Eurocode 2: Design of Concrete Structures—Part 1-1: General Rules and Rules for Buildings*; CEN: Brussels, Belgium, 2006; Volume 1.
26. Urban, T.; Gołdyn, M.; Krawczyk, Ł.; Sowa, Ł. Experimental investigations on punching shear of lightweight aggregate concrete flat slabs. *Eng. Struct.* **2019**, *197*, 109371. [CrossRef]
27. Moreillon, L.; Suter, R.; le Roy, R. Punching shear resistance of Uhpfrc slabs: Experimental works and design model. In Proceedings of the RILEM-Fib-AFGC International Symposium on Ultra-High Performance Fibre-Reinforced Concrete, UHPFRC 2013, Marseille, France, 1–3 October 2013; pp. 577–586.
28. Reis, N.; de Brito, J.; Correia, J.R.; Arruda, M.R.T. Punching behaviour of concrete slabs incorporating coarse recycled concrete aggregates. *Eng. Struct.* **2015**, *100*, 238–248. [CrossRef]
29. Kneubuehl, B.P. *Wound Ballistics: Basics And Applications*; Springer: Berlin/Heidelberg, Germany; New York, NY, USA, 2011.
30. ASTM. *ASTM C1018-97 Standard Test Method for Flexural Toughness and First-Crack Strength of Fiber-Reinforced Concrete (Using Beam With Third-Point Loading)*; ASTM Standard: West Conshohocken, PA, USA, 1997; Volume 04, p. 7. [CrossRef]
31. Hamad, A.J.; Sldozian, R.J.A. Flexural and flexural toughness of fiber reinforced concrete-American Standard specifications review. *Grd. J. Glob. Res. Dev. J. Eng.* **2019**, *4*, 5–13.

32. JSCE. Test method for bending strength and bending toughness of steel fiber reinforced concrete. In *Standard Specification for Concrete Structures. Test Methods and Specifications*; JSCE: Tokyo, Japan, 2005.
33. Francesconi, L.; Pani, L. Punching shear strength of reinforced recycled concrete slabs. In *Insights Innov. Struct. Eng. Mech. Comput.—The 6th International Conference on Structural Engineering, Mechanics and Computation SEMC 2016*; CRC Press/Balkema: Boca Raton, FL, USA, 2016; pp. 1338–1343.

Publisher's Note: MDPI stays neutral with regard to jurisdictional claims in published maps and institutional affiliations.

© 2020 by the authors. Licensee MDPI, Basel, Switzerland. This article is an open access article distributed under the terms and conditions of the Creative Commons Attribution (CC BY) license (http://creativecommons.org/licenses/by/4.0/).